Posted on 25 May 2023 — The copyright holder is the author/funder. All rights reserved. No reuse without permission. — https://doi.org/10.22541/essoar.168500291.18596925/v1 — This a preprint and has not been peer reviewed. Data may be preliminary.

Modeling Kelvin Helmholtz Instability Tube & Knot Dynamics and Their Impact on Mixing in the Lower Thermosphere

Tyler Mixa[1], Thomas Lund[1], and David C. Fritts[1]

[1]GATS

May 25, 2023

Modeling Kelvin Helmholtz Instability Tube & Knot Dynamics and Their Impact on Mixing in the Lower Thermosphere

Tyler S. Mixa[1,2], Thomas S. Lund[2], and David C. Fritts[1,2]

[1]Center for Space and Atmospheric Research (CSAR), Embry-Riddle Aeronautical University
[2]Global Atmospheric Technologies and Sciences (GATS)-inc Boulder

Key Points:

- Tube & knot (T&K) dynamics yield faster, more aggressive instability evolutions than axially uniform KHI in stratified shear environments.
- T&K-induced twist waves drive the turbulent transition and preclude secondary CI/KHI that dominate prior laboratory and simulation studies.
- T&K-induced turbulence yields faster/larger kinetic energy depletion and entropy production, producing more mixing with weaker efficiency.

Corresponding author: Tyler S. Mixa, `tyler@gats-inc.com`

Abstract

We present modeling results of Kelvin Helmholtz Instability (KHI) tube and knot (T&K) dynamics accompanying a thermospheric KHI event captured by the 2018 Super Soaker campaign (Mesquita et al., 2020). Chemical tracers released by a rocketsonde on 26 January 2018 showed a coherent KHI in the lower thermosphere that rapidly deteriorated within 45-90 s. Using wind and temperature data from the event, we conducted high resolution direct numerical simulations (DNS) employing both wide and narrow spanwise domains to facilitate (wide domain case) and prohibit (narrow domain case) the axial deformation of KH billows that allows tubes and knots to form. KHI T&K dynamics are shown to produce accelerated instability evolution consistent with the observations, achieving peak dissipation rates nearly 2 times larger and 1.8 buoyancy periods faster than axially uniform KHI generated by the same initial conditions. Rapidly evolving twist waves are revealed to drive the transition to turbulence; their evolution precludes formation of secondary convective instabilities (CI) and secondary KHI seen to dominate the turbulence evolution in artificially constrained laboratory and simulation environments. T&K dynamics extract more kinetic energy from the background environment and yield greater irreversible energy exchange and entropy production, yet they do so with weaker mixing efficiency due to greater energy dissipation. The results suggest that enhanced mixing from thermospheric KHI T&K events could account for the discrepancy between modeled and observed mixing in the lower thermosphere (Liu, 2021; Garcia et al., 2014) and merits further study.

1 Introduction

On 26 January 2018, a Kelvin-Helmholtz Instability (KHI) event was observed at the unusually high altitude of 102 km by a Rocketsonde chemical tracer release over Poker Flats, Alaska (Mesquita et al., 2020). The KH billows had horizontal wavelengths of $\lambda_h =$ 9.6 km and rapidly deteriorated from their initial coherent state in a scant 45-90 s, indicating an aggressive underlying shear layer with an approximate half depth of $d \approx \lambda_h/4\pi \approx$ 800 m. In-situ Rocketsonde wind profiles revealed an apparent superposition of an inertial gravity wave (GW)-induced shear layer and a smaller-scale shear sheet causing the elevated local shear. Lidar measurements from the Poker Flats Research Range showed a similarly sharp temperature enhancement near the same altitude, yielding a local minimum Richardson number (Ri) of 0.05 consistent with rapid shear turbulence evolution.

Highly localized multi-scale environments comprised of such "sheet and layer" superpositions are found throughout the atmosphere and have been shown to produce instability events yielding widespread turbulence with elevated dissipation (see e.g., Fritts et al., 2017, and citations therein), yet their contributions to larger-scale mixing and chemical constituent distributions remain largely unknown. General circulation models (GCMs) represent mixing with the vertical eddy diffusion coefficient, K_{zz}, which approximates heat fluxes and transport due to gravity wave breaking but does not address mixing contributions from other sources. K_{zz} is estimated by applying linear saturation theory to a GCM's parameterized gravity wave spectra (Garcia et al., 2007; Liu, 2000); it accounts for turbulence localization with inverse Prandtl number scaling (e.g., Fritts & Dunkerton, 1985; McIntyre, 1989) but otherwise neglects nonlinear dynamics and subgrid-scale turbulence. The resulting mixing estimates yield a near-50% deficit from observations: WACCM profiles of gravity wave-parameterized K_{zz} show values of 5-50 m^2 s^{-1} from 80-100 km (Liu, 2021) whereas global mean O density profiles measured by the Scanning Imaging Absorption Spectrometer for Atmospheric Chartography (SCIAMACHY) instrument suggest $K_{zz} \sim$ 10-80 m^2 s^{-1} over 80-100 km (Swenson et al., 2018), a factor of 1.6-2x larger.

Weaker mixing in WACCM mischaracterizes the transport and global distributions of CO_2 and other constituents. CO_2 mixing ratios are consistently too small above 100 km and do not match the observed falloff with altitude (Garcia et al., 2014) . Similarly, Na and Fe transport are both under-estimated in WACCM; fluxes of Na and Fe need to be larger to agree with cosmic dust and ablation models (Gardner, 2018). Several efforts have been made to yield greater mixing in GCMs by incorporating parameterized heat fluxes from propagating gravity waves (Gardner, 2018) and reducing Pr to produce better agreement with observations (Garcia et al., 2014). However, Liu (2021) maintains that subgrid-scale dynamics in the MLT account for the majority of the modeled mixing deficit.

Localized shear turbulence events must be considered as a possible mixing source in the mesosphere and lower thermosphere (MLT) to address this mixing deficiency in GCMs. Sharp wind and temperature gradients such as those underlying the Mesquita event exist throughout the atmosphere at scales below the resolution limit of GCMs, and the resulting Ri-critical shear layers produce local instabilities everywhere they occur. Such events arise in multi-scale environments exhibiting what are described as "sheet and layer" structures, which occur throughout the atmosphere into the MLT and which modeling reveals to be prolific sources of local KHI (Fritts & Wang, 2013; Fritts et al., 2013), see e.g., Kantha et al. (2017); Doddi et al. (2021); Barat (1982); Sato and Woodman (1982); Lehmacher et al. (2011); Mesquita et al. (2020). Though ubiquitous, GCM resolution cannot capture these dynamics (Fritts, Lund, et al., 2022) and their mixing contributions remain unaddressed.

Recent simulations and observations further suggest that many shear-induced instability events undergo "tube and knot" (T&K) dynamics and could account for more mixing than previously attributed to these events. The conventional understanding of KHI evolution assumes billows that are axially uniform, with expected morphologies of turbulence scale progression driven by secondary convective instabilities (CI) forming in the billow cores and secondary KHI in the billow braids (see e.g., Klaassen & Peltier, 1985; Peltier & Caulfield, 2003; Fritts et al., 2014). Real shear layers, however, are not infinitely uniform; variable intensities and depths over their spatial extent will impact the axial coherence of KHI. Laboratory experiments by Thorpe (1987) showed that even in an artificially uniform environment, KHI "tubes" and "knots" arise and intensify between adjacent, misaligned KH billows prior to the evolution of secondary CI and KHI (see e.g., Fritts et al., 2021a). Over 30 years later, observations by Hecht et al. (2021) revealed KHI T&K dynamics occurring in the MLT, and subsequent modeling and a review of other MLT observational evidence revealed these dynamics to be widespread, perhaps even ubiquitous, in the MLT (Fritts et al., 2021a; Fritts, Wang, Lund, & Thorpe, 2022). However, T&K simulations to-date have only occurred in idealized environments that don't directly correspond to observed atmospheric conditions. Given the potential of KHI T&K dynamics to promote elevated mixing in the MLT, it is imperative to investigate the impact of T&K dynamics on observed shear turbulence events to determine if they can account for the missing mixing modeled in the MLT.

In this study, we evaluate the impact KHI T&K dynamics on the 26 January 2018 thermospheric KHI event reported by Mesquita et al. (2020). In approximating the observed KHI dynamics we demonstrate how T&K formation accelerates and intensifies billow turbulence evolution to promote enhanced dissipation and mixing. To isolate T&K influences, identically initialized direct numerical simulations (DNS) of the Mesquita event are conducted with two spanwise (axial) domain sizes: an 8 KHI λ_h domain allowing T&K formation and a 0.5 KHI λ_h domain prohibiting axial non-uniformity. T&K formation is shown to yield rapid proliferation of small-scale turbulent features in places where KH billows link that both form and dissipate at earlier times than the secondary CI/KHI-driven turbulence transition of axially uniform KHI. T&K driven dynamics achieve peak dissipation at twice the speed and amplitude of the equivalent case limited to axially uniform KHI, with similarly enhanced and accelerated mixing. The significant impact of T&K dynamics in this environment suggests extensive contributions to momentum transport and deposition that could aid the development of improved mixing parameterizations in GCMs.

The remainder of the paper is organized as follows: Section 2 presents a description of the numerical methods, including the governing equations, solution method, and simulation parameters employed by our numerical model; the procedure to determine representative initial conditions from the available observations; and the nondimensional parameters defining the simulation environment. Simulation results are presented in Section 3, evaluating the instability characteristics, dissipation and energy exchange, and mixing characteristics promoted by T&K dynamics relative to their absence. Section 4 contains the summary and conclusions of our results.

2 Numerical Methods

2.1 CGCAM Model Architecture

Simulations herein are conducted using the Complex Geometry Compressible Atmosphere Model (CGCAM). CGCAM solves the nonlinear, compressible Navier-Stokes equations, written in divergence form as:

$$\frac{\partial \rho}{\partial t} + \frac{\partial \left(\rho u_j\right)}{\partial x_j} = 0 \tag{1}$$

$$\frac{\partial \left(\rho u_i\right)}{\partial t} + \frac{\partial \left(\rho u_i u_j\right)}{\partial x_j} = -\frac{\partial p}{\partial x_i} - \rho g \delta_{i3} + \frac{\partial \sigma_{ij}}{\partial x_j} \tag{2}$$

$$\frac{\partial \rho E}{\partial t} + \frac{\partial \left[\left(\rho E + p\right) u_j\right]}{\partial x_j} = -\rho g u_3 + \frac{\partial \left(u_i \sigma_{ij}\right)}{\partial x_j} - \frac{\partial q_j}{\partial x_j} \tag{3}$$

where σ_{ij} and q_j are the viscous stress and thermal conduction, defined as

$$\sigma_{ij} = \mu \left[\left(\frac{\partial u_i}{\partial x_j} + \frac{\partial u_j}{\partial x_i} \right) - \frac{2}{3} \left(\frac{\partial u_k}{\partial x_k} \right) \delta_{ij} \right] \quad \text{and} \quad q_j = -\kappa \frac{\partial T}{\partial x_j} \quad . \tag{4}$$

Here μ is the dynamic viscosity, κ is the thermal conductivity, and δ_{ij} is the Kronecker delta. μ and κ depend on the temperature through Sutherland's Law (White, 1974). The solution variables are the air density ρ, the momentum per unit volume ρu_i or $(\rho u, \rho v, \rho w)$ with velocity components $(u_i, u_j, u_k) = (u, v, w)$ along (x, y, z). Energetics and entropy are discussed in Section 3.3.

We assess the evolution of instability features via the vorticity magnitude

$$|\zeta| = |\nabla \times u| \tag{5}$$

and the intermediate eigenvalue λ_2 of the tensor

$$\mathcal{H} = \mathcal{S}^2 + \mathcal{R}^2 \tag{6}$$

(see e.g., Jeong & Hussain, 1995), where $\mathcal{S}$ and $\mathcal{R}$ are the strain and rotation rate tensors, with components defined as

$$\mathcal{S}_{ij} = \frac{1}{2} \left(\frac{\partial u_i}{\partial x_j} + \frac{\partial u_j}{\partial x_i} \right) \quad \text{and} \quad \mathcal{R}_{ij} = \frac{1}{2} \left(\frac{\partial u_i}{\partial x_j} - \frac{\partial u_j}{\partial x_i} \right) \quad . \tag{7}$$

$|\zeta|$ and $|\lambda_2 < 0|$ reveal the dominant features with strong rotational tendencies, enabling the visualization of emerging KHI, T&K, and twist waves as the flow becomes turbulent.

Solution variables are stored at the cell centroids and fluxes on the faces are constructed using a kinetic energy-conserving interpolation scheme similar to that discussed in Felten and Lund (2006) for the incompressible Navier-Stokes equations. The governing equations are discretized using the finite-volume framework, in which each computational cell is considered to be a small control volume. The resulting scheme is globally conservative for mass, momentum, total energy, and kinetic energy. Time advancement is achieved via a low-storage, third-order accurate Runge-Kutta scheme with a variable time step satisfying the CFL stability condition. Additional details for CGCAM are provided by Dong et al. (2020) and Lund et al. (2020).

The model domains employed in these simulations extend 40 km in the streamwise (x) direction (4 KHI λ_h) and from 90 to 115 km in altitude (z). To enable direct comparisons of cases with and without T&K dynamics, DNS were conducted with two spanwise (y, axial) domain sizes: an 80 km (8 KHI λ_h) domain allowing T&K formation and a 5 km (0.5 KHI λ_h) domain prohibiting axial non-uniformity. The domain employs periodic horizontal boundary conditions and characteristic vertical boundary conditions. 2.5 km sponge layers at the top and bottom of the vertical domain constrain the useable domain to $92.5 < z < 112.5$ km. Each simulation is executed on Department of Defense high-performance supercomputers with a (Nx,Ny$_1$,Ny$_2$,Nz) $= (1824, 3648, 228, 1152)$ grid, having streamwise and spanwise grid resolution of $(\Delta x, \Delta y) = 21.9298$ m and $\Delta z =$ 21.7014 m. To seed the instability formation, a white noise spectrum is added to the initial background wind field with a root mean square amplitude of 10^{-3} m s^{-1}.

2.2 Defining Representative Initial Conditions

The observational datasets capturing the Mesquita et al. (2020) KHI event include wind profiles triangulated from the Rocketsonde TMA chemical release, temperature profiles from the nearby Poker Flats Na lidar, and remote imaging of the Rocketsonde chemical tracer release revealing the KHI evolution. Raw profiles from the Rocketsonde and Na lidar (blue curves) and profile decompositions (orange and yellow curves) are shown in Figure 1, and the modified initial conditions for the simulations are shown in Figure 2. Rocketsonde zonal and meridional wind profiles (Figure 1a-b) display rotary tendencies indicating an inertial gravity wave (IGW) with a compressed phase structure generating a narrow region of enhanced local shear near 103 km. Sinusoidal decomposition of the winds (Figure 1a-b) reveal a local 4 km λ_z sinusoidal enhancement (orange curves) superposed with the background 16 km λ_z IGW (yellow curves) underling the peak shear. The nearby Na lidar temperature profile (Figure 1c) shows local maximum at 101 km indicating peak stability 1-2 km lower than the peak shear altitude in the Rocketsonde winds. The temperature profile is spatially offset from the Rocketsonde measurement but roughly coincident in time. Lidar data indicates significant temporal variability, with peak T shifting ± 20 K and ± 2 km in the hour surrounding the event. The dashed line at the top of the profile indicates a region where a low signal to noise ratio could compromise the accuracy of the measured lapse rate. However, lapse rates from the NRLMSISE/00 empirical model employed by Mesquita et al. (2020) conservatively estimate a minimum Richardson number of 0.05 near the KHI altitude.

KHI revealed by the chemical tracer exhibit $\lambda_h = 9.6$ km and rapidly deteriorate in 45-90 s. The underlying layer depth of $d \approx \lambda_h / 4\pi = 800$ m that sourced these KHI is larger than the layer depth in the measured background profiles, suggesting that the initial layers were deeper and higher in amplitude before the KHI began eroding the layer. Suitable layer characteristics to excite these KHI require collocated shear and stability layers of equal characteristic scales with amplitudes that yield the underlying Ri. Given both the altitude offset between wind and temperature layers and the layer depth disagreement between the measured profiles and the observed KHI, a set of composite profiles needs to be generated from the observations to match the KHI event characteristics.

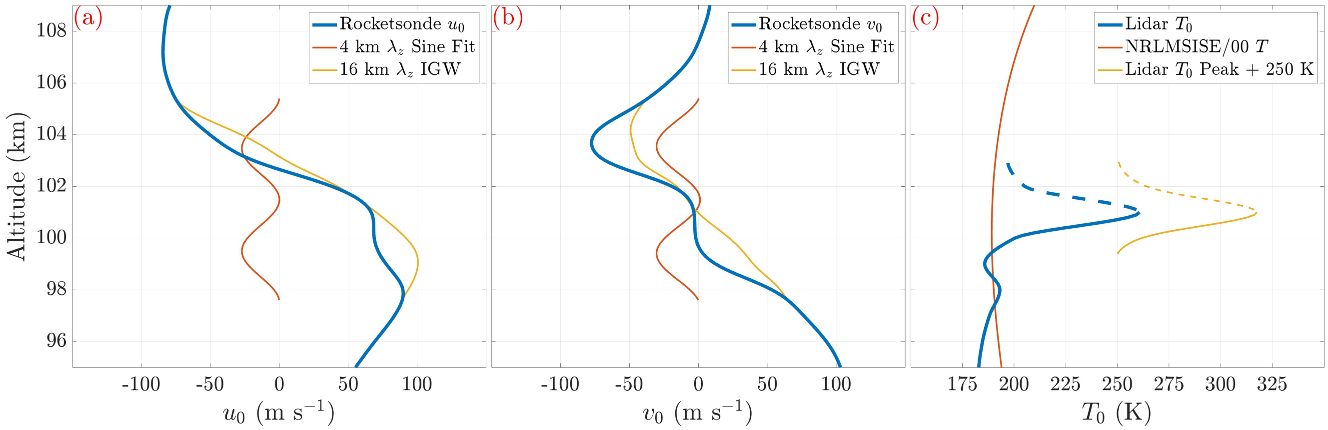

Figure 1. Rocketsonde and Lidar profiles (blue curves) and decompositions (orange and yellow curves) from the Mesquita et al. (2020) KHI event.

When working with non-collocated datasets with different sensitivity to feature evolution, the features of each dataset must be combined in a self-consistent manner that faithfully represents the underlying environmental parameters dictating the event. Adhering to this approach, input wind and temperature profiles were adapted to comprise collocated layers that yield Ri and KHI λ_h characteristics matching the observed instability evolution: (1) An NRLMSISE/00 empirical temperature profile (Figure 1c, orange curve) was subtracted from T_0 to isolate the temperature peak in the lidar data (Figure 1c, yellow curve) corresponding to the sinusoidal local wind enhancement. (2) The lidar temperature peak was then superposed on the model temperature profile at the altitude of peak shear to collocate the layers underlying the KHI. (3) The vertical depths of the temperature peak and 4 km λ_z sinusoidal wind feature were then increased to produce 800 m shear and stability layers matching the observed KHI, and the peak wind/temperature amplitudes were increased/decreased to yield a minimum Richardson number of $Ri =$ 0.05. (4) To retain the initial background characteristics above the layer, wind/temperature profiles above their modified peaks were extended vertically with the same vertical shear ($\partial\{u_0, v_0\}/\partial z$) and stability ($N^2$) found above the initial layers. (5) For numerical convenience, the final wind components were rotated 45° to have maximum shear in the streamwise (x) direction at the layer, and the spanwise (y) component of the rotated winds having minimum shear was set to 0 m s^{-1} to prevent spanwise feature advection. Figure 2 shows the measured wind and stability profiles in the rotated domain ($\widetilde{u}_0, \widetilde{v}_0, N_0^2$) and the resulting modified profiles ($u_{\text{final}}, v_{\text{final}}, N^2_{\text{final}}$) used to initialize CGCAM runs, where u and v are the wind components in the x (streamwise) and y (spanwise) coordinate directions of the simulation domain.

2.3 Derived Layer and Nondimensional Parameters

The layer characteristics of the background profiles are shown in Figure 3, including $\left(\frac{\partial U}{\partial z}\right)^2$, N^2, and Ri. Shear and stability profiles for the collocated layers are shown in Figure 3a-b, with 800 m scaled sech^2 and sech^4 profiles (dashed lines) confirming the layer half depth of the input profiles. The Richardson number is given by

$$Ri = N^2 / \left(\frac{\partial U}{\partial z}\right)^2 \tag{8}$$

and shown in Figure 3c. The minimum value of $Ri = 0.05$ occurs at the layer center at 102.9 km.

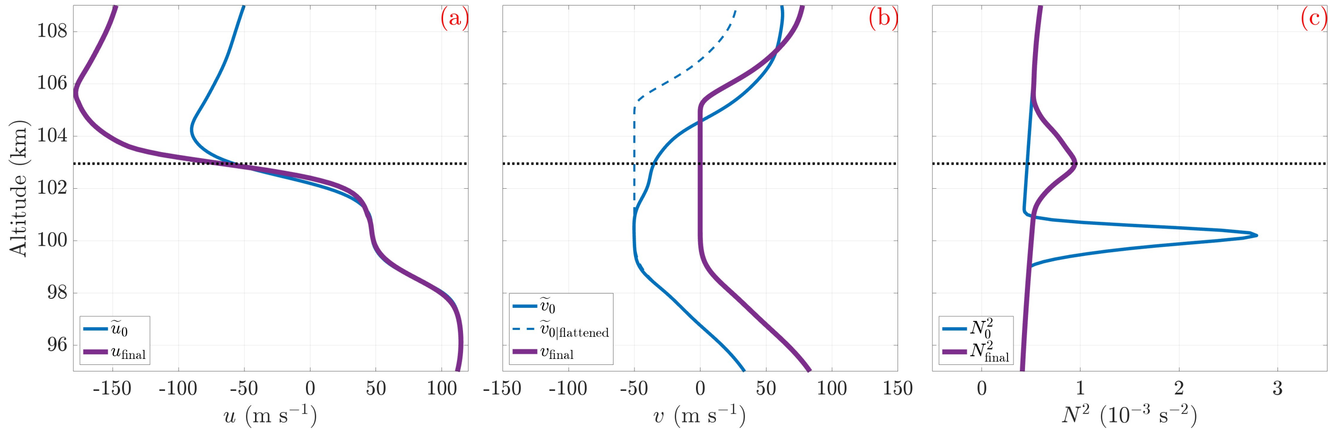

Figure 2. Original and modified background profiles of u, v, and N used to initialize the simulations. Variables are plotted in the rotated coordinate frame of the simulation domain.

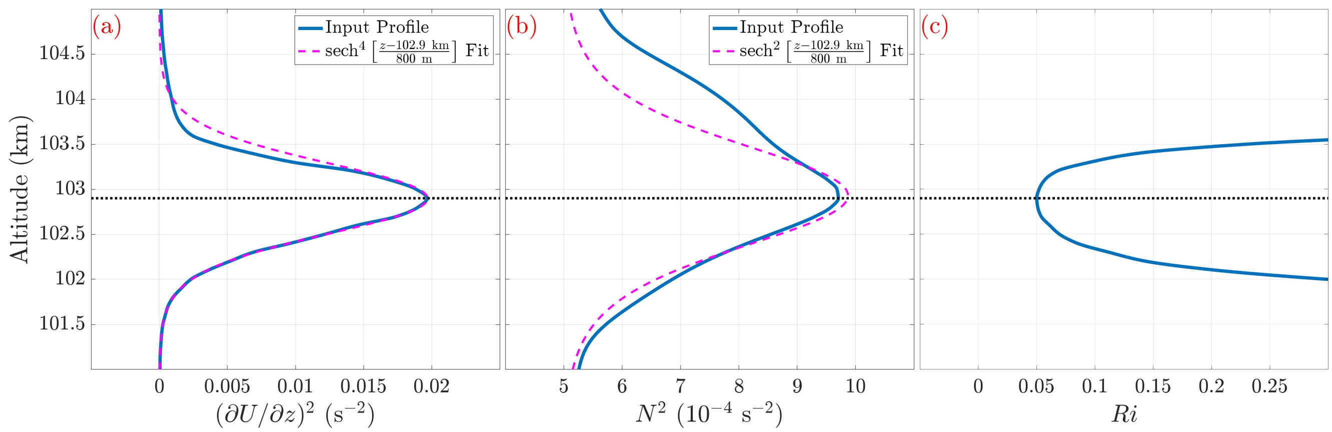

Figure 3. Profiles of the vertical shear $\left(\frac{\partial U}{\partial z}\right)^2$, stability N^2, Richardson number Ri, and their associated 800 m fits.

The Reynolds number is calculated from the shear layer half depth d as

$$Re = \frac{\rho \; d\Delta U/2}{\mu} \quad , \tag{9}$$

where ΔU is the velocity difference over the shear layer and μ is the kinematic viscosity. μ is calculated via Sutherlands Law (White, 1974) from the ground reference value $\mu_0 = 1.506 \times 10^{-5}$ m^2 s^{-1} and the background temperature and density. Peak values of $Re = 2200$ at the layer support the formation of both secondary CI and secondary KHI for this low Ri.

Simulations indicated peak horizontally-averaged kinetic energy dissipation rates per unit mass of $\epsilon_m =$ 2-3 W kg^{-1} and a corresponding Kolmogorov length scale of

$$\eta = \left(\nu^3/\epsilon_m\right)^{\frac{1}{4}} \approx 12 \text{ m} \quad . \tag{10}$$

The domain grid spacing of $\Delta\mathbf{x} \approx 22$ m results in a resolution ratio of $R = \Delta\mathbf{x}/\eta = 1.83$ which satisfies the DNS criteria of $R \approx 1.5$-2.1 (Moin & Mahesh, 1998; Pope, 2000). Hence, true DNS is achieved and no subgrid-scale turbulence parameterization is required.

3 Results

The purpose of the numerical results is to demonstrate how T&K features follow distinct instability pathways that evolve faster, dissipate more energy, and yield more mixing than axially uniform KHI. Section 3.1 presents the instability morphologies of the T&K-allowing DNS, showing how misaligned billow junctions and axial non-uniformity lead to T&K feature superpositions that quickly become turbulent and engulf the domain. Section 3.2 identifies the equivalent instability evolutions in a smaller horizontal domain consistent with previous KHI DNS, where the narrower spanwise dimension precludes axial billow deformations that would otherwise enable T&K dynamics. Here the turbulence is dominated by characteristic secondary CI/KHI and billow pairing as seen in previous studies, dynamics that are precluded by the rapid evolution of T&K-induced dissipation in the wider domain DNS. Section 3.3 compares the dominant dissipation, entropy, and energy exchange metrics in both DNS, demonstrating how both instantaneous and integrated metrics mirror the dominant instability features and yield larger values for the T&K case. Section 3.4 introduces and evaluates the mixing efficiency of both events using a several standard metrics, showing how T&K dynamics produce more mixing but do so at weaker assessed efficiencies.

3.1 Instability Differentiation with T&K

Horizontal overviews (Figure 4) of the vorticity magnitude $|\zeta|$ and intermediate eigenvalue λ_2 in the T&K-allowing DNS reveal spanwise KH billow deformation sites exciting T&K evolutions and twist waves. The horizontal domain is presented in a parallelogram orientation, shifting the center location of the periodic streamwise domain from $x = 0$ km to $x = \pm 20$ km along the spanwise extent of the domain. This display format retains the full extent of the x-y domain in a single plot while elucidating the relative locations of vorticity features straddling the streamwise boundaries. Along the spanwise axis, initial KH billows in panel 1 exhibit local variations in $|\zeta|$ orientation leading to lateral junctions where adjacent billows are misaligned. These distorted billow regions form characteristic T&K structures consistent with (Fritts, Wang, Lund, & Thorpe, 2022; Fritts, Wang, Thorpe, & Lund, 2022) that locally elevate $|\zeta|$:

1. horizontally rotated KH billows produce "billow linking" vortex tubes connecting pairs of streamwise-adjacent billows at marked locations T1-T6; and
2. regions where 2 billows link to 1 (2:1) produce "billow merging" vortex knots in a loop connecting the three spanwise-adjacent billows at marked locations K1-K4.

Each site identified in panel 2 hosts a unique superposition of T&K features connecting up to 5 adjacent KH billows:

- Sites S1 and S5 have a vortex knot with a vortex tube linking one leg of the knot to the adjacent billow at larger x;
- Site S2 has a vortex knot with a vortex tube linking one leg to the adjacent upstream billow and another vortex tube linking the knot core to the adjacent downstream billow;
- Site S3 has two vortex tubes linking the central billow to both the upstream and downstream billows; and
- Site S4 has a vortex knot with a vortex tube shared with S3 linking the knot core to the adjacent upstream billow.

All five T&K superposition sites break down the parent vortices into mode 1 and mode 2 Kelvin vortex waves referred to here as twist waves (Kelvin, 1880), instability structures comprising radial displacements that rotate along the vortex axis as they propagate away from the initial location. Mode 1 twist waves start with a single radial dis-

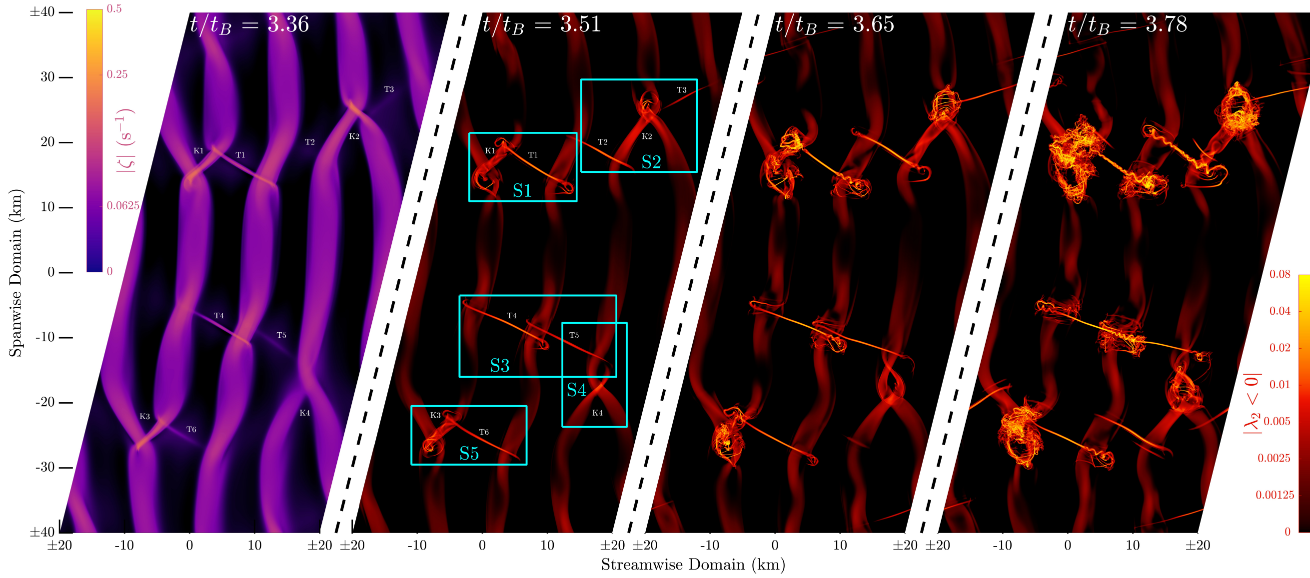

Figure 4. Horizontal cross-sections of the vorticity magnitude (ζ, left) and rotational vorticity component (λ_2, right panels) showing T&K evolution from 3.36-3.78 t_B. Labeled features are described in the text. See video in supplemental materials for additional times.

placement that distorts a cylindrical vortex filament into a helix as it propagates, and mode 2 twist waves split the vortex filament with a pair of radial displacements that differentially advect each other to form a double helix. Panels 2-4 of Figure 4 exhibit several characteristic twist wave evolutions for similar sets of T&K feature superpositions. Billow linking vortex tubes (T1-T6) produce pairs of mode 1 twist waves that propagate from the linked billows toward the tube centers in panels 3-4. Billow merging vortex knots having one leg linked to an adjacent billow at Sites S1, S2, and S5 form mode 2 twist waves in the linked leg of the knot (intersection K1-T1 at S1 and intersection K3-T6 at S5 in panels 2-4; intersection T2-K2 at S2 in panels 3-4) Larger mode 2 twist waves also form at Sites S2 and S4 on the single-leg side of 2:1 knots K2 and K4. Knot cores (K1-K4) also exhibit fragmentation as small scale, adjacent vortices become intertwined. All of these processes yield finer scale, higher amplitude vorticity structures that drive the transition to turbulence.

Instability sites produced by T&K dynamics generate local, rapidly expanding turbulence regions that quickly engulf the entire horizontal extent of the shear layer. Figure 5 shows horizontal overviews of the event in the manner of Figure 4 demonstrating the evolution of widespread turbulence from the initial T&K sites (a full video can be found in the supplemental materials). Initial billow distortions in panel 1 quickly develop T&K features that develop mode 1 and mode 2 twist waves (panel 2). Mode 2 twist waves and the interaction of mode 1 twist wave with adjacent, orthogonal KHI cause fragmentation of KH billow cores. Twist wave-induced fragmentation yields smaller scale, intensified vortical structures, and successive like interactions drive the transition to turbulence as they proliferate in all directions from their source sites (panel 3). Losing their initial anisotropy, regions of intense turbulence merge and entrain most of the shear layer into large, well-mixed regions. Turbulence regions promoted by T&K dynamics are notably more aggressive than streamwise swaths of near-axial uniformity at $y = 0$ and $y = \pm 40$ km, suggesting that T&K dynamics yield more vigorous and intensified turbulence than KHI events constrained to be axially uniform. The evolutions and linkages that lead to intensified T&K dynamics appear to preclude the potential for secondary CI seen in the axially uniform KHI at later times.

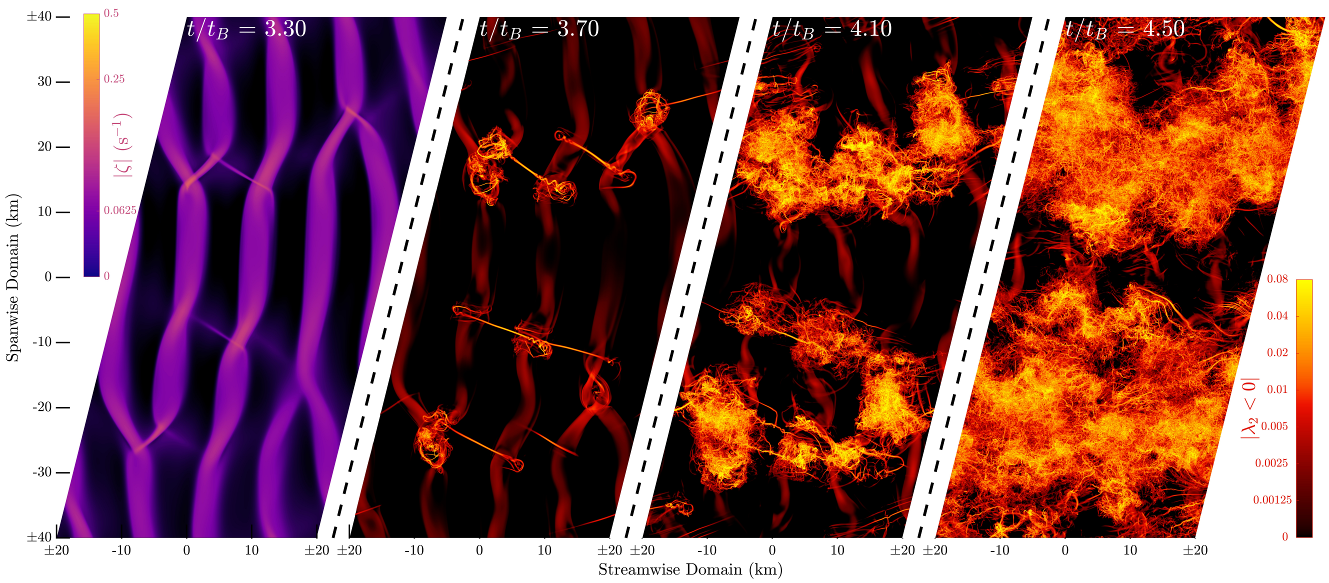

Figure 5. As in Figure 4 for 3.30-4.50 t_B.

3.2 Instability Evolution in Axially Uniform KHI

Comparing KHI cross sections from the T&K-allowing DNS with the T&K-prohibiting DNS conclusively shows the radical departures of T&K evolutions from equivalently initialized, axially uniform KHI. Streamwise-vertical slices (Figure 6a-d) of the temperature perturbations (T') at $y = 20$ km in the T&K-allowing DNS reveal the following crucial deviations from domain center T' slices in the T&K-prohibiting DNS (Figure 6e-h) at the same times:

1. Though initial KHI in both cases (Figure 6a,e) evolve at similar times and scales, KHI in the T&K-allowing cross-section develop secondary instability structures (Figure 6b) while the T&K-prohibiting KHI remain coherent (Figure 6f).
2. At the latter two times (Figure 6c-d and g-h), the T&K-allowing case is already well-mixed by the time the T&K-prohibiting case shows signs of weak tertiary instability structures in the periphery of the billow cores.

w' and T' cross-sections of the T&K-prohibiting DNS in Figure 7 reveal billow merging that delays secondary CI/KHI formation and elicits stirring oscillations within the billow cores. Billow merging at 4.76 t_B (Figure 7b,f) reduces the number of KHI billows in the streamwise domain from 4 to 3. As the two central billows merge, their perturbation amplitudes weaken relative to earlier times (Figure 7a,e), further delaying instability onset. Spanwise cross-sections at $z = 103$ km show no indications of secondary CI formation until after 4.76 t_B (Figure 7i-l), long after turbulence has fully engulfed the T&K-allowing domain in Figure 6. Prominent secondary KHI form at the top of the billows at 5.61 t_B (Figure 7d,h), driving the transition to turbulence a full 2 t_B after the initial billow formation. Within the billows, peak amplitude regions of T' (w') in the billow core advect horizontally (vertically) about the vertical (horizontal) billow core axis rather than immediately dissipating. These oscillatory motions delay the fully mixed state of horizontal homogeneity to much later times as the entrained fluid stirs about the bil-

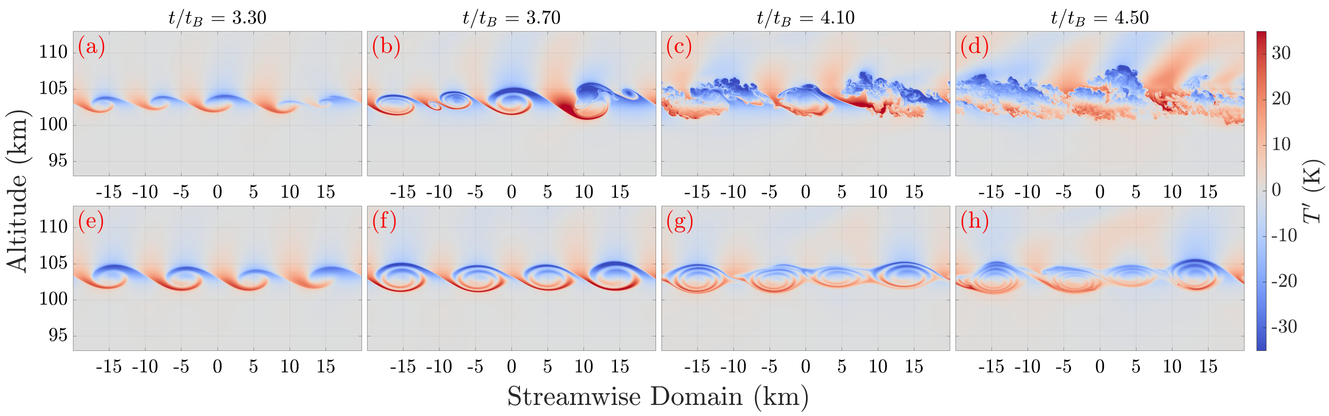

Figure 6. Vertical cross-sections of the temperature perturbation (T') fields comparing KHI evolution in the T&K-allowing (top) and T&K-prohibiting (bottom) DNS results. Times correspond to the four panels in Figure 5.

low core for several buoyancy periods (a full video can be found in the supplemental materials).

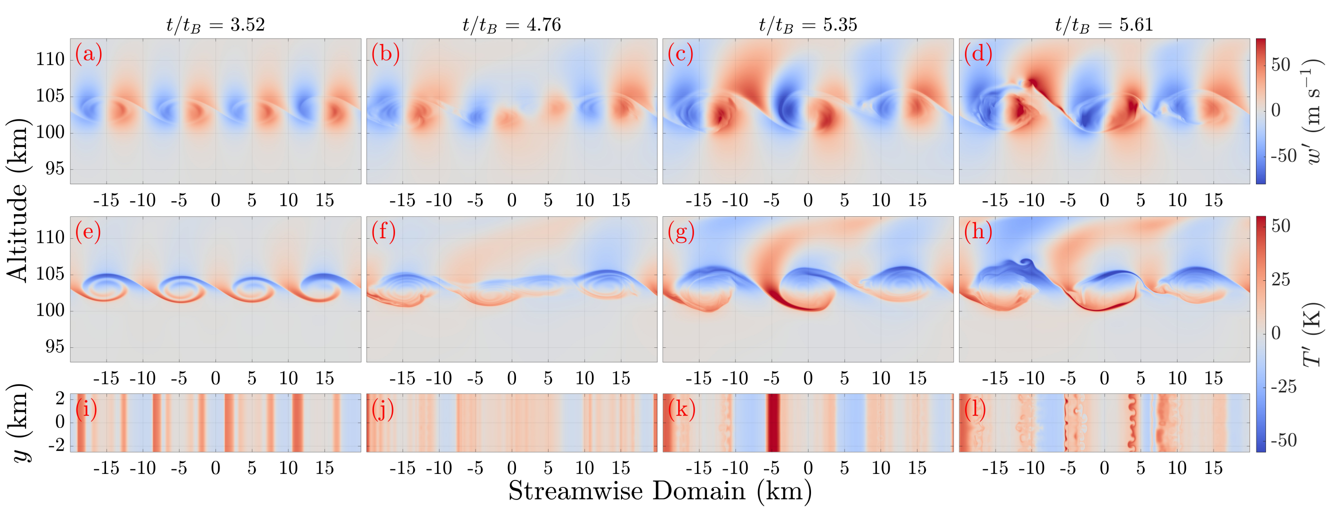

Figure 7. Vertical w' cross-sections (top), vertical T' cross-sections (middle), and horizontal T' cross-sections (bottom) in the T&K-prohibiting DNS results.

3.3 Dissipation and Energy Exchange Differentiation with T&K

To evaluate turbulence and mixing characteristics, we compare the dominant terms of entropy creation and energetic exchange in the two DNS cases. The production of volume-averaged entropy, neglecting boundary fluxes, is given by

$$\Delta S = \int \left(\left\langle \frac{\epsilon}{T} \right\rangle + \left\langle \frac{\chi}{T^2} \right\rangle \right) dt \quad , \tag{11}$$

where $\epsilon = \sigma_{ij}\mathcal{S}_{ij}$ is the kinetic energy dissipation rate, $\chi = k\left(\frac{\partial T}{\partial x_k}\frac{\partial T}{\partial x_k}\right)$ is the thermal energy dissipation rate, and $\langle\rangle$ indicates volume averaging. $\mathcal{E} = \langle\epsilon\rangle$ is a marker for the onset of 3D turbulence, while $\mathcal{X} = \langle \chi \rangle$ is an approximate metric for perturbation amplitude growth in the dominant instabilities. The volume-averaged total energy is given by

$$E = KE + PE + IE \quad , \tag{12}$$

where $KE = \langle \rho u_k u_k / 2 \rangle$ is the volume-averaged kinetic energy, $PE = \langle \rho g z \rangle$ is the volume-averaged potential energy, $IE = c_v \langle T \rangle$ is the volume-averaged internal energy, and c_v is the specific heat at constant volume. We also assess mixing via energy exchange from kinetic energy to potential and internal energy:

$$\Delta KE_{|KE \Longleftrightarrow PE} = \int \mathcal{W}_b \; dt \quad , \tag{13}$$

where $\mathcal{W}_b = \langle \rho g w' \rangle$ is the volume-averaged buoyancy work, and

$$\Delta KE_{|KE \Longleftrightarrow IE} = \int \left(\mathcal{E} - \mathcal{W}_{pv} \right) dt \quad , \tag{14}$$

where $\mathcal{W}_{pv} = \left\langle p \frac{\partial u_k}{\partial x_k} \right\rangle$ is the volume-averaged pressure-volume work. Here we note that of the energy exchange quantities, only ϵ represents a positive-definite, irreversible ($\rightharpoonup$) depletion of KE; $\mathcal{W}_b$ and $\mathcal{W}_{pv}$ both constitute bidirectional energy exchange ($\Longleftrightarrow$), but their final equilibrium states ($\rightleftharpoons$) can be assessed as irreversible work once turbulence subsides.

Figure 8 shows the time evolution of $\mathcal{E}$, $\mathcal{X}$, and $\mathcal{W}_b$ for both DNS. Faster instability evolution in the T&K-allowing case yields more vigorous dissipation: T&K-driven turbulence achieves a peak dissipation rate of $\mathcal{E} = 4.95 \times 10^{-7}$ W m^{-3} at 4.91 t_B, 94% larger and 1.8 t_B earlier than the secondary CI/KHI-driven turbulence in the T&K-prohibiting DNS ($\mathcal{E} = 2.55 \times 10^{-7}$ W m^{-3} at 6.68 t_B). These results expand on the dissipation analysis of Fritts, Wang, Lund, and Thorpe (2022); Fritts, Wang, Thorpe, and Lund (2022) and definitively disprove the long-held notion that secondary CI are the primary trigger of enhanced dissipation in stratified shear environments (see e.g., Klaassen & Peltier, 1985; Caulfield & Kerswell, 2000; Peltier & Caulfield, 2003, and citations therein). $\mathcal{X}$ evolutions identify rapid instability amplitude growth accompanying the $\mathcal{E}$ peak in the T&K-allowing DNS, but $\mathcal{X}$ in the T&K-prohibiting DNS is markedly different, decreasing after its initial increase at ~ 3 t_B until the onset of elevated $\mathcal{E}$ at ~ 6 t_B. The decrease is correlated with the billow merging identified in Figure 7, showing how merging and slower secondary CI/KHI growth delay dissipation to later times in the absence of T&K dynamics. $\mathcal{W}_b$ in the T&K-allowing DNS is predominantly positive, but it is dwarfed by the periodic positive and negative oscillations in the T&K-prohibiting DNS after 5 t_B. These $\mathcal{W}_b$ oscillations correspond to stirring motions identified in Figure 7 (panels c-d; g-h) for the T&K-prohibiting DNS; though the oscillations have higher absolute amplitudes than in the T&K-allowing DNS, a significant portion of $\mathcal{W}_b$ in the T&K-prohibiting DNS is reversible and does not contribute to the net mixing in the final state of the flow.

Accumulated mixing parameters in Figure 9 show markedly higher event-level dissipation, entropy production, and kinetic energy conversion enabled by T&K dynamics. Comparable final states are identified by equivalent $\mathcal{E}$ values, where the T&K-allowing DNS produces 33% larger accumulated $\mathcal{E}$, 12% larger accumulated $\mathcal{X}$, and 30% larger ΔS than the T&K-prohibiting DNS. ΔKE is also 19% larger in the T&K-allowing DNS, driven primarily by larger and faster $\mathcal{E}$ growth. The partitioned KE exchanges (last two panels) are both non-monotonic, indicating reversible exchanges via positive $\mathcal{W}_{pv}$ and negative $\mathcal{W}_b$. Time evolution of the $KE \Longleftrightarrow IE$ energy exchange shows an initial KE increase in both cases (negative values) due to elevated $\mathcal{W}_{pv}$ during the initial KHI rollup. The duration and amplitude of $IE \implies KE$ are larger in the T&K-prohibiting DNS due to the longer duration of KHI billow coherence, but both cases eventually produce net $KE \rightharpoonup IE$ after the onset of turbulence. The $KE \Longleftrightarrow PE$ exchange confirms that much of the $\mathcal{W}_b$ in the T&K-prohibiting case after 5 t_B is reversible; though it achieves

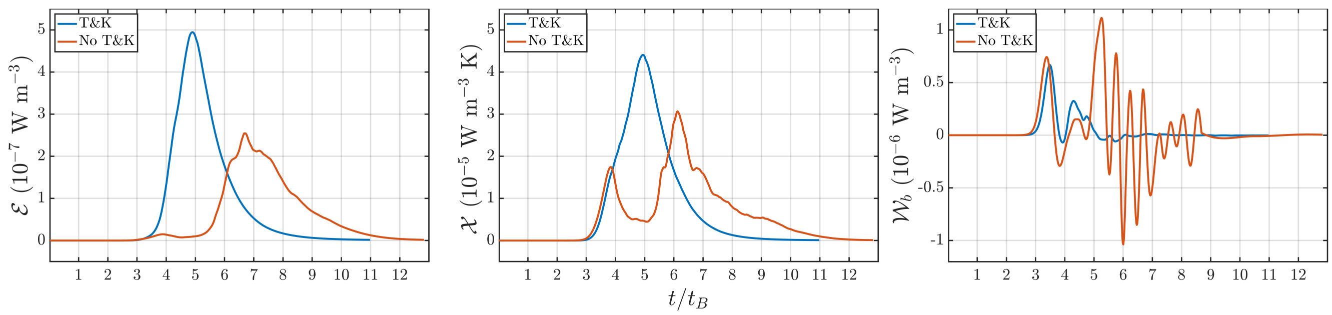

Figure 8. Instantaneous domain-averaged mixing parameters for the T&K-allowing and T&K-prohibiting DNS.

a larger accumulated $KE \Longrightarrow PE$ at 6 t_B, the final $KE \rightleftharpoons PE$ state restores the stirred energy back to KE, producing a $KE \rightharpoonup PE$ deficit of 4% relative to the T&K-allowing case. The mixing implications of these results are discussed below.

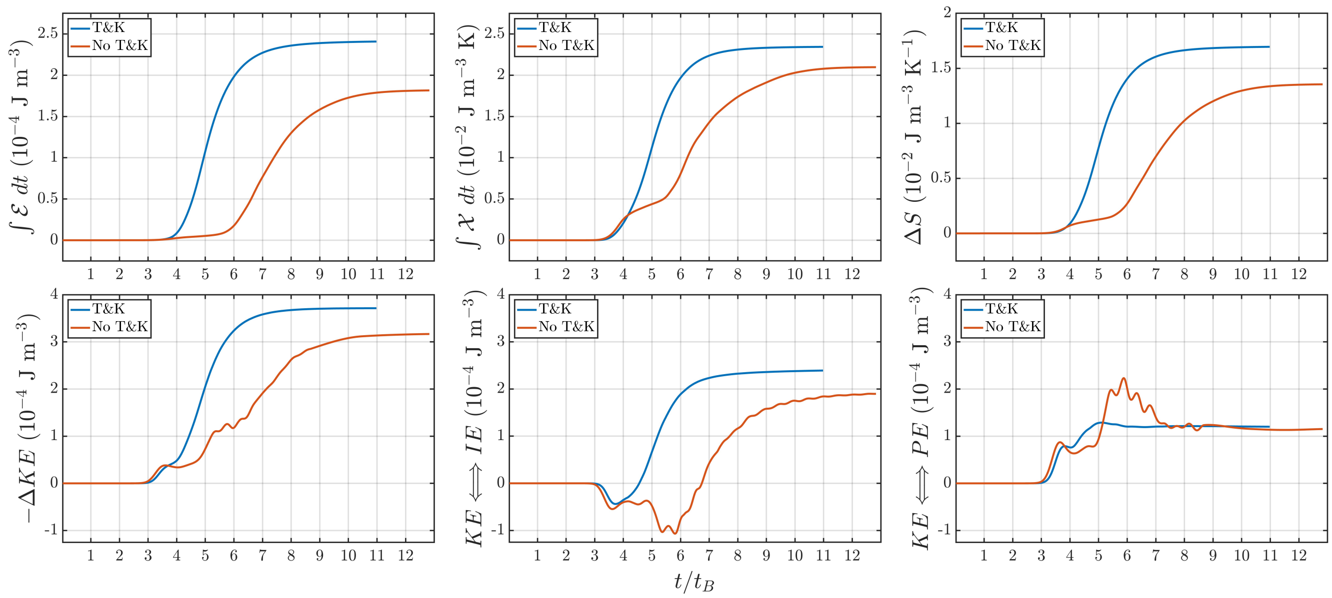

Figure 9. Integrated domain-averaged mixing parameters for the T&K-allowing and T&K-prohibiting DNS, including the resulting ΔS, ΔKE, and the partitioned KE exchanges with IE and PE.

3.4 Mixing Efficiency Differentiation with T&K

Broadly, the mixing efficiency γ of a turbulence event is assessed as a ratio of the increase in potential energy to the expended kinetic energy in the final equilibrium state, i.e.

$$\gamma_E = \frac{\Delta PE}{-\Delta KE} \tag{15}$$

(Gregg et al., 2018). Though K_{zz} is useful as an aggregate atmospheric measure in GCMs, γ is the more suitable tool for assessing DNS and can be estimated with K_{zz} from GCMs or observations via the equilibrium assumption methods of T. R. Osborn and Cox (1972) or those of Weinstock (1978); T. Osborn (1980). Equation 15 is often simplified to

$$\gamma_{\mathcal{W}} = \frac{\int \mathcal{W}_b \; dt}{\int \mathcal{E} \; dt} \tag{16}$$

with the similarly derived flux Richardson number R_f expressed as

$$R_{f|\mathcal{W}} = \frac{\int \mathcal{W}_b \; dt}{\int \left(\mathcal{W}_b + \mathcal{E}\right) dt} \tag{17}$$

to be bounded by 1. In Boussinesq flows, Equations 16 and 17 represent the net energy exchanges $KE \rightleftharpoons PE$ and $KE \rightleftharpoons IE$ in the final equilibrium state. The equivalent expressions for a compressible environment are then

$$\gamma_{KE} = \frac{\int \mathcal{W}_b \; dt}{\int \left(\mathcal{E} - \mathcal{W}_{pv}\right) dt} \quad \text{and} \quad R_{f|KE} = \frac{\int \mathcal{W}_b \; dt}{\int \left(\mathcal{W}_b + \mathcal{E} - \mathcal{W}_{pv}\right) dt} \tag{18}$$

utilizing the ΔKE partition in Equations 13-14. Winters et al. (1995) proposed the alternate metric of available potential energy

$$APE = \rho g(z - z_*) \tag{19}$$

to isolate the irreversible mixing at the end state of $KE \rightleftharpoons PE$ in Boussinesq flows, representing the potential energy released when a disturbed density profile adiabatically returns to a monotonically decreasing (z_*) state. Tailleux (2009, 2013) later showed that the volume-averaged net dissipation of APE can be expressed in compressible flows as the time average

$$\overline{D}_{APE} = \overline{\mathcal{W}}_b - \overline{\mathcal{W}}_{pv} \tag{20}$$

over the duration of the event. The resulting mixing parameters are given by

$$\gamma_{APE} = \frac{\overline{D}_{APE}}{\overline{\mathcal{E}}} \quad \text{and} \quad R_{f|APE} = \frac{\overline{D}_{APE}}{\overline{D}_{APE} + \overline{\mathcal{E}}} \quad , \tag{21}$$

We can also assess irreversible mixing efficiency with the entropy production constituents via

$$\gamma_S = \frac{\int \left\langle \chi / T^2 \right\rangle dt}{\int \left\langle \epsilon / T \right\rangle dt} \quad \text{and} \quad R_{f|S} = \frac{\int \left\langle \chi / T^2 \right\rangle dt}{\Delta S} \quad . \tag{22}$$

These mixing assessments and their input parameters are shown together in Table 1 as an event summary for both cases.

The resulting mixing efficiency parameters demonstrate both increased energetic extraction and reduced efficiency of extraction where T&K dynamics occur. The most direct efficiency assessment yields $\gamma_E \approx 0.3$ for both DNS, consistent with the typical range of $\gamma_E = 0.2 - 0.3$ seen in atmospheric and oceanic observations (see e.g., Gregg et al., 2018; Lozovatsky & Fernando, 2013, and citations therein). The T&K-allowing DNS generates 10% more PE than the T&K-prohibiting DNS in its final state, but it does so with 7% lower γ_E due to its 19% larger ΔKE. The flux-based $\gamma_{\mathcal{W}}$ and ΔKE partition-based γ_{KE} indicate a higher mixing efficiency of 0.5-0.63, with $R_{f|\mathcal{W}}$ and $R_{f|KE}$ values of 0.33-0.39 closer to γ_E. The inclusion of $\mathcal{W}_{pv}$ in γ_{KE} and $R_{f|KE}$ yields mild efficiency reductions in the T&K-prohibiting case owing to net negative $\mathcal{W}_{pv}$ work, which increases the assessed available flux energy when compressible effects are considered. The 21-27% reduced $\gamma_{\{\mathcal{W},KE\}}$ and 12-14% reduced $R_{f|\{\mathcal{W},KE\}}$ in the T&K-allowing DNS stem from 26-33% larger extractions of $\mathcal{E}$ and $KE \rightharpoonup IE$ with only slightly (4%) larger $\int \mathcal{W}_b$. The dissipation based metrics γ_{APE} and $R_{f|APE}$ and entropy-based metrics γ_S and $R_{f|S}$ have comparable efficiency ranges ($\gamma \approx$ 0.5-0.7, $R_f \approx$ 0.3-0.4) to the flux and KE partition-based metrics, with the T&K-prohibiting case having slightly higher γ_{APE} and slightly lower γ_S. As with the other efficiency metrics, the 16-27% lower $\gamma_{\{APE,S\}}$ and 11-18% lower $R_{f|\{APE,S\}}$ in the T&K-allowing event suggest weaker mixing despite having 18%

Table 1. Event Mixing Efficiency Parameters

Parameter	Unit	T&K Prohibited	T&K Allowed	% Change[a]
ΔPE	J m^{-3}	9.21×10^{-5}	1.02×10^{-4}	+10.43%
ΔKE	J m^{-3}	-3.17×10^{-4}	-3.75×10^{-4}	+18.50%
γ_E	–	0.29	0.27	−6.81%
$\int \mathcal{W}_b \, dt$	J m^{-3}	1.15×10^{-4}	1.20×10^{-4}	+4.20%
$\int \mathcal{E} \, dt$	J m^{-3}	1.82×10^{-4}	2.41×10^{-4}	+32.60%
$\gamma_{\mathcal{W}}$	–	0.63	0.50	−21.42%
$R_{f\|\mathcal{W}}$	–	0.39	0.33	−14.29%
$\int (\mathcal{E} - \mathcal{W}_{pv}) \, dt$	J m^{-3}	1.90×10^{-4}	2.39×10^{-4}	+26.00%
γ_{KE}	–	0.61	0.50	−27.30%
$R_{f\|KE}$	–	0.38	0.33	−11.52%
$\overline{D}_{APE}$	W m^{-3}	3.45×10^{-8}	4.08×10^{-8}	+18.27%
$\overline{\mathcal{E}}$	W m^{-3}	5.13×10^{-8}	8.33×10^{-8}	+62.40%
γ_{APE}	–	0.67	0.49	−27.17%
$R_{f\|APE}$	–	0.40	0.33	−18.23%
$\int \langle \chi \,/\, T^2 \rangle \, dt$	J m^{-3} K^{-1}	4.28×10^{-7}	5.38×10^{-7}	+11.61%
$\int \langle \epsilon \,/\, T \rangle \, dt$	J m^{-3} K^{-1}	8.73×10^{-7}	1.16×10^{-6}	+32.62%
γ_S	–	0.55	0.46	−15.84%
$R_{f\|S}$	–	0.36	0.32	−10.82%

[a]Calculated with respect to the T&K Prohibited value as 100%.

greater $\overline{D}_{APE}$ and 12% greater $\int \langle \chi/T^2 \rangle$. These varied mixing efficiency assessments ultimately fail to capture the heightened energetic exchange, dissipation, and entropy production occurring in T&K events.

A more suitable mixing efficiency comparison between the two cases can be constructed by isolating the reversible components of their net energy exchange terms. Figure 10 shows the total $KE \Longleftrightarrow IE$ and $KE \Longleftrightarrow PE$ energy transfers for both cases decomposed into positive ($KE \Longrightarrow$) and negative ($KE \Longleftarrow$) components of integrated $(\mathcal{E}{-}\mathcal{W}_{pv})$ and $\mathcal{W}_b$. Since both transfers are net positive, the cancelled-out negative energy transfer indicates how much of the positive energy transfer is reversed in the final state and can be assessed as a mixing inefficiency. In $KE \rightleftharpoons PE$, $KE \leftharpoondown PE$ represents vertically displaced particles returning from their displaced altitude rather than dissipating. In $KE \rightleftharpoons IE$, $KE \leftharpoondown IE$, represents compressed regions adjacent to the expanding billows returning to their original pressure and volume as the KHI dissipate and mix with the surrounding fluid. These components reveal vastly larger reversed (i.e. wasted) energy transfers in the T&K-prohibiting DNS, where 44% of $KE \rightharpoonup IE$ is reversed (vs. 16%) and 63% of $KE \rightharpoonup PE$ is reversed (vs. 10%). As a mixing efficiency metric, the amount of retained energy transfer can be expressed as

$$\gamma_{\{IE,PE\}} = \frac{KE \rightleftharpoons \{IE,PE\}}{KE \rightharpoonup \{IE,PE\}} \quad \text{and} \quad R_{f|\{IE,PE\}} = \frac{KE \rightleftharpoons \{IE,PE\}}{KE \rightharpoonup \{IE,PE\} - KE \leftharpoondown \{IE,PE\}} \quad , \tag{23}$$

where the values for the T&K-prohibiting (allowing) DNS are $\gamma_{IE} = 0.56$ $(0.84, +50\%)$, $R_{f|IE} = 0.39$ $(0.73, +87\%)$, $\gamma_{PE} = 0.37$ $(0.90, +143\%)$, and $R_{f|PE} = 0.22$ $(0.81, +268\%)$.

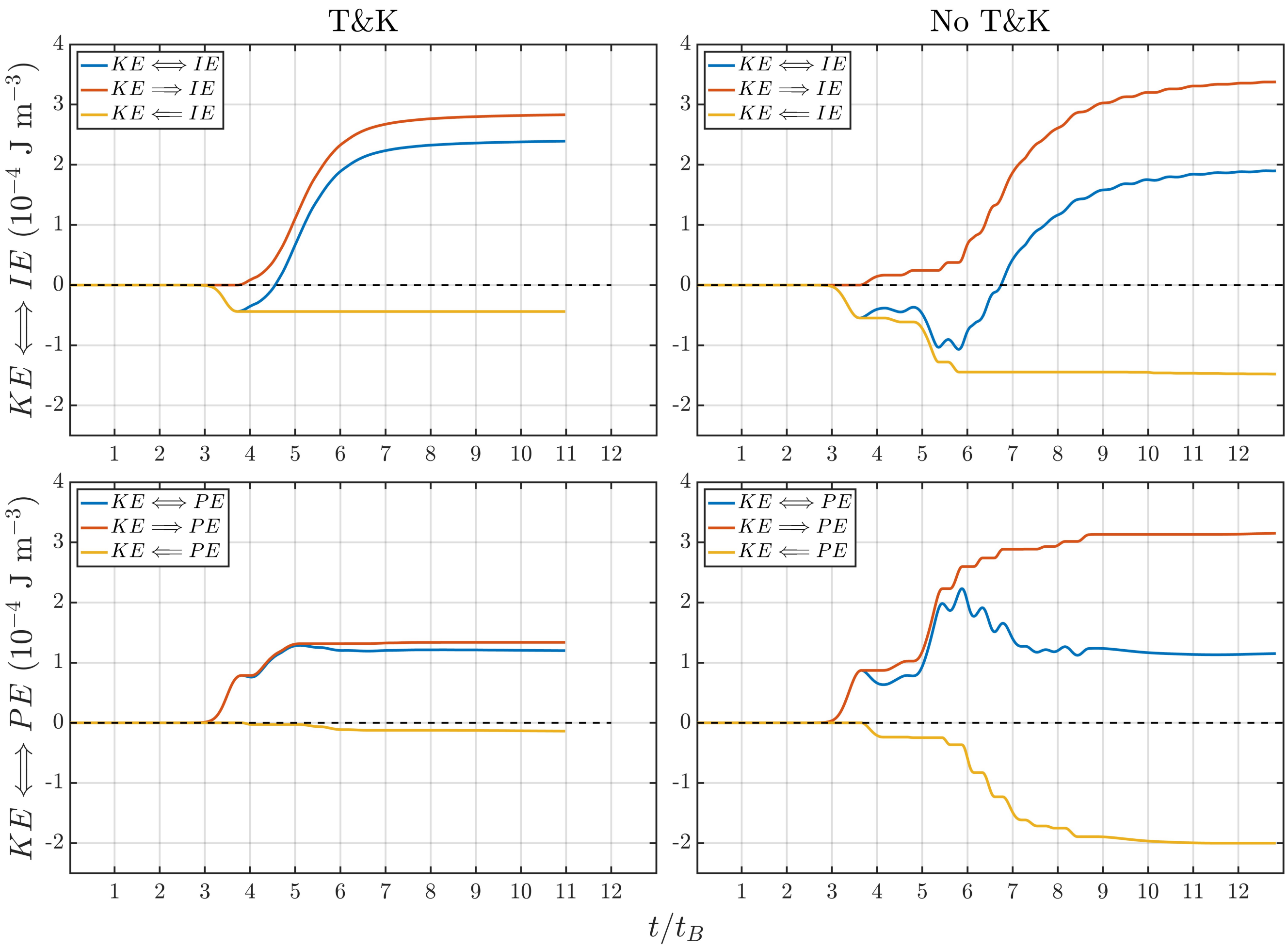

Figure 10. Comparing total ($\Longleftrightarrow$), positive ($\Longrightarrow$), and negative ($\Longleftarrow$) components of integrated energy transfer from KE with and without T&K.

4 Summary and Conclusions

DNS presented in this study evaluate the impact of T&K dynamics on a thermospheric KHI event observed on 26 January 2018 over Poker Flats, Alaska. The instability event was triggered by elevated shear and temperature perturbations from a local 4 km λ_z shear/stability enhancement superposed on a 16 km λ_z background IGW. Initial conditions generated from available observations reproduced the underlying 800 m layer having $Ri_{\min} = 0.05$ and $Re = 2200$. Identically initialized DNS were conducted in two spanwise box sizes to assess the instability and mixing consequences when KHI are not constrained to axial uniformity as in prior studies.

DNS allowing T&K dynamics reveal unique instability pathways that evolve faster turbulence transitions and yield more vigorous dissipation and mixing than morphologies evolving from axially uniform KHI. Spanwise-billow distortions and misaligned billow junctions seed superpositions of billow linking vortex tubes and billow merging vortex knots consistent with morphologies identified by (Fritts, Wang, Lund, & Thorpe, 2022; Fritts, Wang, Thorpe, & Lund, 2022). These superposed T&K features develop mode 1 and mode 2 twist wave evolutions that fragment their parent features into smaller intertwined vortex filaments with further elevated magnitudes. This rapid progression to small scales stemming from initial T&K sites yields expanding turbulence regions that quickly engulf the entire horizontal extent of the shear layer.

Cross-section comparisons with axially uniform KHI show T&K dynamics having faster fine-scale feature evolution and locally larger dissipation. Faster turbulence precludes the development of billow merging and secondary CI/KHI, dominant evolutions in the T&K-prohibiting case and previously thought to ubiquitously drive the turbulent transition in all stratified shear turbulence scenarios. In the absence of T&K, weaker turbulence damps dissipation as fluid parcels are repeatedly stirred about the billow core rather than mixed.

The resulting macro-scale dissipation and energy exchanges conclusively quantify the capacity for T&K instability events to contribute to elevated mixing in the thermosphere and beyond, with far-reaching implications. T&K dynamics produce 94% (44%) larger peak $\mathcal{E}$ ($\mathcal{X}$) values 1.8 t_B (1.2 t_B) faster than axially uniform KHI. Billow pairing and slowly evolving secondary CI/KHI in the T&K-prohibiting DNS yield oscillating $\mathcal{W}_b$ and weaker, stepped evolutions of $\mathcal{E}$ and $\mathcal{X}$. Over the whole event, T&K dynamics accumulate 19% more ΔKE, 33% more $\mathcal{E}$, 26% more $KE \rightleftharpoons IE$, 62% more $\overline{\mathcal{E}}$, and 30% more ΔS than the T&K-prohibiting DNS, but they only yield 10% more ΔPE, 4% more $KE \rightleftharpoons PE$, 18% more $\overline{D}_{APE}$, and 12% more $\mathcal{X}$. Consequently, γ and R_f values are $7-27$% smaller and $11-18$% smaller, respectively, in the T&K-allowing DNS despite displaying more mixing in every assessed standard metric. However, it is noteworthy that the T&K-allowing DNS retains a much greater fraction of its reversible energy exchanges (50% greater γ_{IE}, 143% greater γ_{PE}), suggesting that other mixing metrics may be valuable for assessing the relative impact of different instability dynamics in the same environment.

The results of this study demonstrate that T&K dynamics dominate the turbulent transition, extracting more energy and entropy more quickly from an existing background environment than idealized, axially uniform KHI. T&K-induced twist waves, not secondary CI/KHI, are shown to be the primary drivers of turbulence and dissipation in atmospheric shear-driven flows. As such, studies of artificially constrained, axially uniform KHI in narrow spanwise lab and simulation experiments severely underestimate the mixing implications of KHI and inflate the importance of secondary CI/KHI and billow pairing in atmospheric and oceanic flows. T&K events produce stronger mixing than axially uniform KHI but do so with reduced efficiency, converting a lower fraction (but larger net amount) of the available kinetic energy into potential energy. Standard mixing efficiency metrics do not capture the enhanced irreversible mixing of T&K events, suggesting that more evaluation is needed of prevailing mixing metrics and available energy concepts to capture T&K impacts in GCM turbulence parameterizations.

5 Open Research

The full domain 3-D data sets used in this study are too large to download from the DoD HPCMP centers, but the datasets and associated scripts used to generate the figures in this paper are publicly available online in the Figshare Data Repository via `https://doi.org/10.6084/m9.figshare.22814600.v1`.

Acknowledgments

Research described here was supported by MURI Grant FA9550-18-1-0009 and NSF Grant AGS-2230482. Poker Flats lidar data was provided by Bifford Williams. We also acknowledge the support of the DoD High Performance Computing Modernization Program (HPCMP) for access to several supercomputer platforms that enabled the simulations reported here.

References

Barat, J. (1982). Some characteristics of clear-air turbulence in the middle stratosphere. *Journal of Atmospheric Sciences*, *39*(11), 2553–2564.

Caulfield, C. P., & Kerswell, R. R. (2000). The nonlinear development of three-dimensional disturbances at hyperbolic stagnation points: A model of the braid region in mixing layers. *Physics of Fluids*, *12*(5), 1032–1043. doi: 10.1063/1.870358

Doddi, A., Lawrence, D., Fritts, D., Wang, L., Lund, T., Brown, W., ... Kantha, L. (2021). Instabilities, dynamics, and energetics accompanying atmospheric layering (ideal) campaign: High-resolution in situ observations above the nocturnal boundary layer. *Atmospheric Measurement Techniques Discussions*, 1–33.

Felten, F. N., & Lund, T. S. (2006). Kinetic energy conservation issues associated with the collocated mesh scheme for incompressible flow. *J. Comp. Physics*, *215*, 465–484. doi: 10.1016/j.jcp.2005.11.009

Fritts, D. C., Baumgarten, G., Wan, K., Werne, J. A., & Lund, T. S. (2014). Quantifying kelvin-helmholtz instability dynamics observed in noctilucent clouds: 2. modeling and interpretation of observations. *Journal of Geophysical Research: Atmospheres*, *119*, 9359-9375. doi: 10.1002/2014JD021833

Fritts, D. C., & Dunkerton, T. J. (1985). Fluxes of heat and constituents due to convectively unstable gravity waves. *Journal of Atmospheric Sciences*, *42*(6), 549–556.

Fritts, D. C., Lund, A. C., Lund, T. S., & Yudin, V. (2022). Impacts of limited model resolution on the representation of mountain wave and secondary gravity wave dynamics in local and global models. 1: Mountain waves in the stratosphere and mesosphere. *Journal of Geophysical Research: Atmospheres*, *127*(9), e2021JD035990.

Fritts, D. C., & Wang, L. (2013). Gravity wave–fine structure interactions. part ii: Energy dissipation evolutions, statistics, and implications. *Journal of the Atmospheric Sciences*, *70*, 3735-3755. Retrieved from `http://journals.ametsoc.org/doi/abs/10.1175/JAS-D-13-059.1` doi: 10.1175/JAS-D-13-059.1

Fritts, D. C., Wang, L., Baumgarten, G., Miller, A. D., Geller, M. A., Jones, G., ... Vinokurov, J. (2017). High-resolution observations and modeling of turbulence sources, structures, and intensities in the upper mesosphere. *Journal of Atmospheric and Solar-Terrestrial Physics*, 1-22. Retrieved from `http://linkinghub.elsevier.com/retrieve/pii/S1364682616304126` doi: 10.1016/j.jastp.2016.11.006

Fritts, D. C., Wang, L., Lund, T., & Thorpe, S. (2022). Multi-scale dynamics of kelvin–helmholtz instabilities. part 1. secondary instabilities and the dynamics of tubes and knots. *Journal of Fluid Mechanics*, *941*, A30.

Fritts, D. C., Wang, L., Thorpe, S., & Lund, T. (2022). Multi-scale dynamics of kelvin–helmholtz instabilities. part 2. energy dissipation rates, evolutions and statistics. *Journal of Fluid Mechanics*, *941*, A31.

Fritts, D. C., Wang, L., & Werne, J. A. (2013). Gravity wave–fine structure interactions. part i: Influences of fine structure form and orientation on flow evolution and instability. *Journal of the Atmospheric Sciences*, *70*, 3710-3734. doi: 10.1175/jas-d-13-055.1

Fritts, D. C., Wieland, S. A., Lund, T. S., Thorpe, S. A., & Hecht, J. H. (2021a). Kelvin-helmholtz billow interactions and instabilities in the mesosphere over the andes lidar observatory: 2. modeling and interpretation. *J. Geophys. Res. Atmos.*, *126*. doi: 10.1029/2020JD033412

Garcia, R. R., López-Puertas, M., Funke, B., Marsh, D. R., Kinnison, D. E., Smith, A. K., & González-Galindo, F. (2014, 5). On the distribution of co2 and co in the mesosphere and lower thermosphere. *Journal of Geophysical Research*, *119*, 5700-5718. doi: 10.1002/2013JD021208

Garcia, R. R., Marsh, D. R., Kinnison, D. E., Boville, B. A., & Sassi, F. (2007, 5). Simulation of secular trends in the middle atmosphere, 1950-2003. *Journal of Geophysical Research Atmospheres*, *112*. doi: 10.1029/2006JD007485

Gardner, C. S. (2018, 6). Role of wave-induced diffusion and energy flux in the vertical transport of atmospheric constituents in the mesopause region. *Journal of Geophysical Research: Atmospheres*, *123*, 6581-6604. doi: 10.1029/2018JD028359

Gregg, M. C., D'Asaro, E. A., Riley, J. J., & Kunze, E. (2018). Mixing efficiency in the ocean. *Annual Review of Marine Science*, *10*(September 2017), 443–473. doi: 10.1146/annurev-marine-121916-063643

Hecht, J. H., Fritts, D. C., Gelinas, L. J., Rudy, R. J., Walterscheid, R. L., & Liu, A. Z. (2021). Kelvin-helmholtz billow interactions and instabilities in the mesosphere over the andes lidar observatory: 1. observations. *Journal of Geophysical Research: Atmospheres*, *126*. doi: 10.1029/2020JD033414

Jeong, J., & Hussain, F. (1995). On the identification of a vortex. *J. Fluid Mech.*, *285*, 69-94.

Kantha, L., Lawrence, D., Luce, H., Hashiguchi, H., Tsuda, T., Wilson, R., ... Yabuki, M. (2017). Shigaraki uav-radar experiment (shurex): overview of the campaign with some preliminary results. *Progress in Earth and Planetary Science*, *4*(1), 1–26.

Kelvin, W. (1880). (1880), vibrations of a columnar vortex. *Phil. Mag.*, *10*, 155-168.

Klaassen, G., & Peltier, W. (1985). The onset of turbulence in finite-amplitude kelvin–helmholtz billows. *Journal of Fluid Mechanics*, *155*, 1–35.

Lehmacher, G., Scott, T., Larsen, M., Bilén, S., Croskey, C., Mitchell, J., ... Collins, R. (2011). The turbopause experiment: atmospheric stability and turbulent structure spanning the turbopause altitude. In *Annales geophysicae* (Vol. 29, pp. 2327–2339).

Liu, H. L. (2000, may). Temperature changes due to gravity wave saturation. *Journal of Geophysical Research Atmospheres*, *105*(D10), 12329–12336. doi: 10.1029/2000JD900054

Liu, H. L. (2021). Effective vertical diffusion by atmospheric gravity waves. *Geophysical Research Letters*, *48*, 1-10. doi: 10.1029/2020GL091474

Lozovatsky, I., & Fernando, H. (2013). Mixing efficiency in natural flows. *Philosophical Transactions of the Royal Society A: Mathematical, Physical and Engineering Sciences*, *371*(1982), 20120213.

McIntyre, M. E. (1989). On dynamics and transport near the polar mesopause in summer. *Journal of Geophysical Research: Atmospheres*, *94*(D12), 14617–14628.

Mesquita, R. L., Larsen, M. F., Azeem, I., Stevens, M. H., Williams, B. P., Collins, R. L., & Li, J. (2020). In situ observations of neutral shear instability in the statically stable high-latitude mesosphere and lower thermosphere during quiet geomagnetic conditions. *Journal of Geophysical Research: Space Physics*, *125*, 1-14. Retrieved from `https://doi.org/10.1029/2020JA027972` doi: 10.1029/2020JA027972

Moin, P., & Mahesh, K. (1998). Direct numerical simulation: A tool in turbulence research. *Annual Review of Fluid Mechanics*, *30(539)*, 78-xx.

Osborn, T. (1980). Estimates of the local rate of vertical diffusion from dissipation measurements. *Journal of physical oceanography*, *10*(1), 83–89.

Osborn, T. R., & Cox, C. S. (1972). Oceanic fine structure. *Geophysical Fluid Dynamics*, *3*(4), 321–345.

Peltier, W., & Caulfield, C. (2003). Mixing efficiency in stratified shear flows. *Annual review of fluid mechanics*, *35*(1), 135–167.

Pope, S. B. (2000). *Turbulent flows* (Vol. 1). Cambridge University Press. doi: 10.1017/CBO9780511840531

Sato, T., & Woodman, R. F. (1982). Fine altitude resolution observations of stratospheric turbulent layers by the arecibo 430 mhz radar. *Journal of Atmospheric Sciences*, *39*(11), 2546–2552.

Swenson, G., Yee, Y., Vargas, F., & Liu, A. (2018, 10). Vertical diffusion transport of atomic oxygen in the mesopause region consistent with chemical losses and continuity: Global mean and inter-annual variability. *Journal of Atmospheric and Solar-Terrestrial Physics*, *178*, 47-57. doi: 10.1016/j.jastp.2018.05.014

Tailleux, R. (2009). On the energetics of stratified turbulent mixing, irreversible thermodynamics, Boussinesq models and the ocean heat engine controversy. *Journal of Fluid Mechanics*, *638*, 339–382. doi: 10.1017/S002211200999111X

Tailleux, R. (2013). Irreversible compressible work and available potential energy dissipation in turbulent stratified fluids. *Physica Scripta*, *88*(T155). doi: 10.1088/0031-8949/2013/T155/014033

Thorpe, S. A. (1987). Transitional phenomena and the development of turbulence in stratified fluids: a review. *J. Geophys. Res.*, *92*, 5231–5248.

Weinstock, J. (1978). Vertical turbulent diffusion in a stably stratified fluid. *Journal of Atmospheric Sciences*, *35*(6), 1022–1027.

White, F. M. (1974). *Viscous fluid flow*. McGraw-Hill, New York.

Winters, K. B., Lombard, P. N., Riley, J. J., & D'Asaro, E. A. (1995). Available potential energy and mixing in density-stratified fluids. *Journal of Fluid Mechanics*, *289*, 115–128.